RSC Advances

PAPER

View Article Online
View Journal | View Issue

Cite this: *RSC Adv.*, 2021, **11**, 7238

Impact of synthesis route on structural, magnetic, magnetocaloric and critical behavior of $Nd_{0.6}Sr_{0.4}MnO_3$ manganite

M. Jeddi, *[a] J. Massoudi, [a] H. Gharsallah,[ab] Sameh I. Ahmed,[c] E. Dhahri [a] and E. K. Hlil[d]

$Nd_{0.6}Sr_{0.4}MnO_3$ polycrystalline manganite was synthesized by two different methods: the auto-combustion reaction (NSMO-AC) and the sol–gel method (NSMO-SG). The structural, magnetic, magnetocaloric and critical behavior of the samples were examined. Rietveld refinements of the XRD patterns revealed that both compounds are pure single phase indexed to the orthorhombic system adopting the *Pnma* space group. The nanometric size estimated using the Williamson–Hall method was confirmed by TEM micrographs. Magnetic measurements as a function of temperature indicated that both samples underwent a second order ferromagnetic (FM)–paramagnetic (PM) phase transition at Curie temperature (T_C). The relative cooling power was observed to be around 95.271 J kg^{-1} for NSMO-AC and 202.054 J kg^{-1} for NSMO-SG at $\mu_0 H = 5$ T, indicating that these materials are potential candidates for magnetic refrigeration application close to room temperature. The critical behavior was estimated using diverse techniques based on the isothermal magnetization data recorded around the critical temperature T_C. The calculated values are fully satisfactory to the requirements of the scaling theory, implying their reliability. The estimated critical exponents matched well with the values anticipated for the mean-field model and the 3D Ising model for NSMO-AC and NSMO-SG, respectively, showing that the magnetic interactions depended on the process of elaboration.

Received 30th November 2020
Accepted 25th January 2021

DOI: 10.1039/d0ra10118d

rsc.li/rsc-advances

1. Introduction

The serious environmental problems and daily energy demands are crucial subjects that whetted the interest of the scientific and engineering communities, with a view of creating new nontoxic, inexpensive, stable, and efficient technologies to solve these issues.[1] Based on the magnetocaloric effect (MCE), magnetic refrigeration is regarded as the new potential cooling technology that is environmentally friendly and energy efficient.[2,3] The MCE is defined as the tendency of the magnetic system to cool down or heat up owing to the variation in the magnetic field.[4] This type of refrigeration has drawn a great deal of attention from several researchers for its promising applications near room temperature, its high efficiency, as well as its ecological cleanliness.[5] Notably, it significantly competes with the conventional gas-compression refrigeration, which is normally responsible for damaging our living environment.[6]

Nowadays, intensive research activities attempt to explore new magnetic materials presenting optimal magnetocaloric properties near room temperature as the most efficient refrigerant materials in the field of magnetic cooling technologies.[7–9] Perovskite-based manganites of compositional formula $(RE_{1-x}A_x)MnO_3$, where RE is a trivalent rare earth atom and A is a divalent alkaline earth one,[10–12] can be considered as good competitors for other magnetocaloric materials. This interest is due to their powerful ability to be exploited in different fields.[13–20] There are several robust arguments that emphasize the fact that this class of compounds will fulfill an impressive contribution in the emerging technologies[21] given that their critical temperature can be adjusted by substitution; their preparation is relatively easy and their cost is lower than that of gadolinium, which is considered as a reference.[22–24] Among these materials, only lanthanum manganites have been fully characterized with a deeper investigation into the structural and magnetic properties.[25–27] Neodymium-based manganites seem to be very promising magnetocaloric candidates[28,29] owing to the reason that the magnitude of their magnetic entropy change and the value of their transition temperature can be strongly tuned by controlling their microstructure and their chemical composition following the preparation method.[30]

As the magnetocaloric properties of manganites were examined only to a limited extent, the exploration of other

[a]*Laboratoire de Physique Appliquée, Faculté des Sciences, Université de Sfax, B. P. 1171, 3000 Sfax, Tunisia. E-mail: marwajeddi@gmail.com*

[b]*Institut Préparatoire aux Études d'Ingénieur de Sfax, Université de Sfax, B. P. 1172, 3018 Sfax, Tunisia*

[c]*Department of Physics, College of Science, Taif University, P. O. Box 11099, Taif 21944, Saudi Arabia*

[d]*Institut Néel, CNRS, Université J. Fourier, B. P. 166, 38042 Grenoble, France*

systems and new elaboration process inducing an improvement in the magnetocaloric effect is still under the initial stage.[31,32] Different methods, such as solid state reaction,[33–36] chemical co-precipitation,[37–39] and sol–gel method[40–43] are available for the synthesis of RE manganites with a perovskite-like structure. The methods of synthesis play a significant role in the formation of the required crystal structure, the control of the crystallite size, and the contribution of magnetic interactions.

The sol–gel route is a classic soft chemistry process, mainly explored in the context of nanometric manganites, which lead to convincing results in terms of particle size. However, calcination is an important step to induce the good crystallization of materials and to remove foreign impurities. This step determines the final dimension of objects and generates sintering phenomena.[44,45] The auto-combustion reaction cannot be described as a soft chemistry process as the temperatures reached during autoignition are very high. However, the fact that the transition from the liquid state to the solid state is very fast allows access to crystallized and single-phase materials with very small sizes, which eliminate the need for a subsequent annealing step.[46,47] Therefore, this phenomenon would constitute a major advantage as far as the sol–gel process is concerned. The synthesis by auto-combustion is a promising technique because it is fast and requires simple equipment and low processing time. It favors high product crystallinity, homogeneous chemical composition, small particle size and narrow particle size dispersion.[48] The reagents are inexpensive, the dopants can be easily integrated into the final product, and multiple steps are not involved.

Motivated by these considerations, a detailed investigation of the structural, magnetic, magnetocaloric, and critical behavior of strontium-doped neodymium manganite $Nd_{0.6}Sr_{0.4}MnO_3$ synthesized by the auto-combustion process and the sol–gel method is reported.

2. Experiment

2.1. Synthesis

The $Nd_{0.6}Sr_{0.4}MnO_3$ sample was prepared using two different methods: the auto-combustion reaction (NSMO-AC) and the sol–gel method (NSMO-SG).

Auto-combustion reaction (NSMO-AC). In this process (Fig. 1a),[49,50] the nitrate reagents, $Nd(NO_3)\cdot 6H_2O$, $Sr(NO_3)_2$, and $Mn(NO_3)_2\cdot 6H_2O$, were dissolved in distilled water, and the solution was kept under magnetic stirring for 1 h and heated on a hot plate at about 100 °C until the mixture turned into a transparent and homogenous solution. The chelating agent used was glycine ($C_2H_5NO_2$), which was added at a molar ratio of 1 : 1 (nitrate : glycine).[51] During heating, the water gradually vaporized, and a transparent viscous gel was formed. At a critical temperature (≈350 °C), autoignition occurred and the combustion lasted for only a few seconds. Relatively, plenty of foam was produced. Finally, the obtained powder was preheated at 700 °C for about 30 min to eliminate the residual organic matter and sintered at 800 °C for 12 h and pressed into pellets.

Sol–gel method (NSMO-SG). The sol–gel method (Fig. 1b) had almost the same processing steps as the auto-combustion preparation. The differences between these two preparation methods were the chelating agent used and the heat treatment. Herein, with the sol–gel method, about same quantities of the previous raw materials were dissolved in distilled water. Subsequently, citric acid ($C_6H_8O_7$) and ethylene glycol ($C_2H_6O_2$) were added in order to obtain a transparent solution. The mixed solution was heated at 80 °C to remove excess water. Then, a viscous glassy gel was formed. On further heat treatment at 120 °C, the obtained gel transformed to dark grayish flakes, which were calcined at 700 °C for 12 h. Finally, the powder was sintered at 800 °C for 12 h and pressed into pellets.

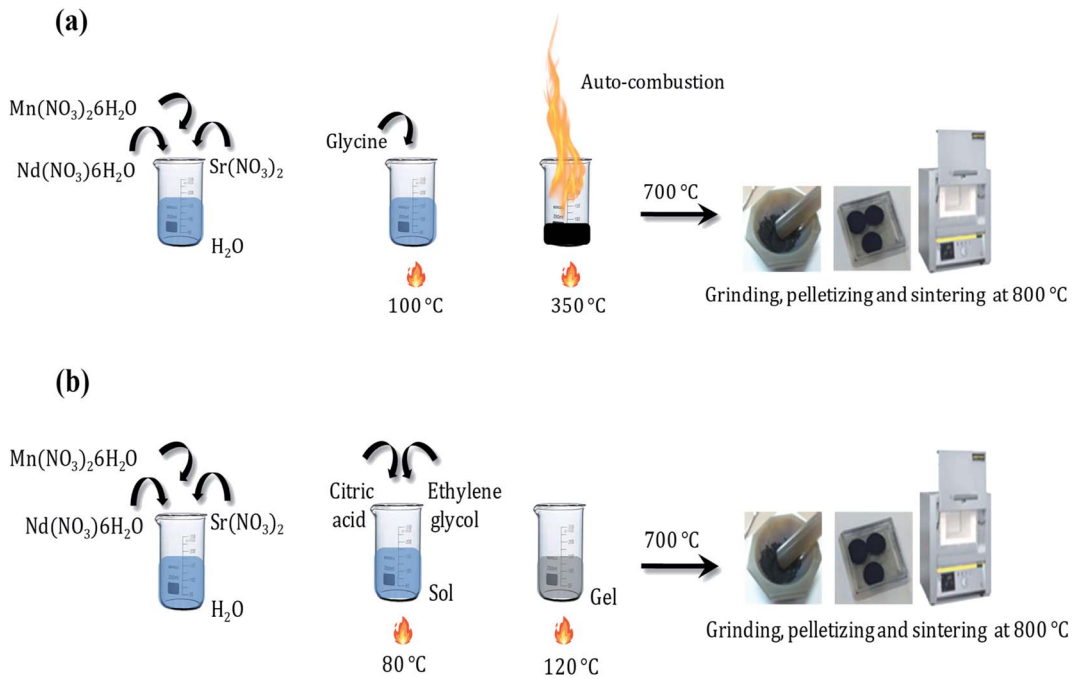

Fig. 1 Summarized procedure of the synthesis of compounds by (a) auto-combustion reaction and (b) sol–gel method.

2.2. Characterization

The XRD patterns of NSMO-AC and NSMO-SG compounds were recorded at room temperature by using the powder X-ray diffraction technique with CuK_α radiation ($\lambda = 1.5406$ Å). The data were collected in the range of $20° \leq 2\theta \leq 80°$ by a step scanning of 0.015°. The structure and phase purity were examined by using the FullProf program.[52] The surface morphology observation and the grain size determination were performed using transmission electron microscopy (TEM). The elemental composition of the elaborated specimens was verified by the energy dispersive X-ray analysis (EDAX). The measurements of magnetization *versus* temperature $M(T)$ were obtained under an applied magnetic field of 0.05 T at a temperature ranging from 5 to 350 K. The measurements of magnetization *versus* magnetic field $M(\mu_0 H)$ were carried out at different temperatures with the magnetic fields varying from 0 to 5 T.

3. Results and discussion

3.1. Structural and morphological study

Fig. 2a introduces the Rietveld refinements of the XRD patterns of NSMO-AC and NSMO-SG samples synthesized by the auto-combustion reaction and the sol–gel method, respectively. Both compounds are single phase without any detectable foreign impurities. The diffraction peaks are satisfactorily crystallized in

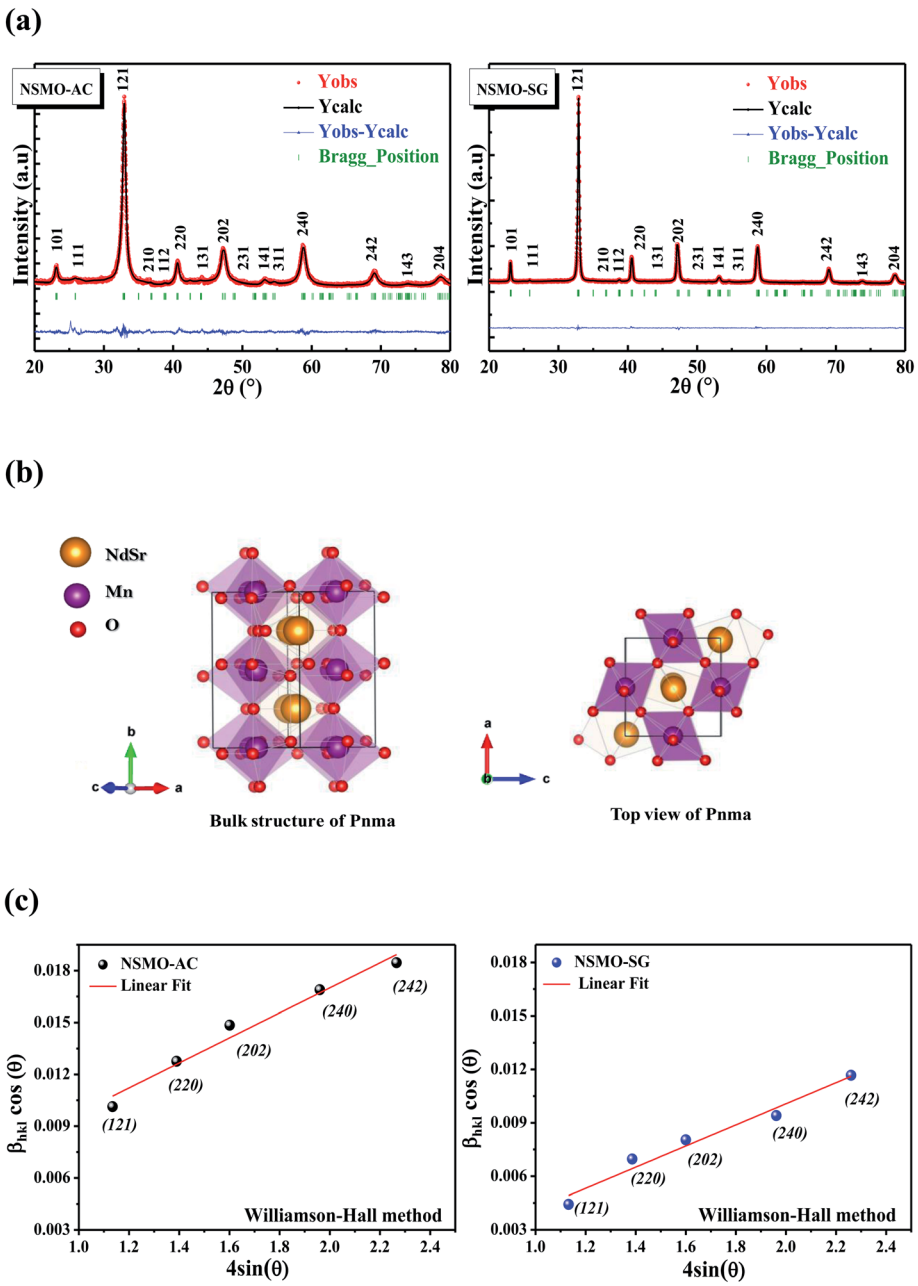

Fig. 2 (a) Rietveld refinement of the X-ray diffraction patterns, (b) crystal structure and (c) Williamson–Hall plot of NSMO-AC and NSMO-SG compounds.

Table 1 Results of the Rietveld refinement for NSMO-AC and NSMO-SG samples

Compound	NSMO-AC	NSMO-SG
Space group	*Pnma*	*Pnma*
a (Å)	5.44243	5.44086
b (Å)	7.66322	7.68139
c (Å)	546654	5.46634
V (Å^3)	227.990	228.457
$\langle d_{Mn-O} \rangle$ (Å)	1.96	1.95
$\langle \theta_{Mn-O-Mn} \rangle$ (°)	160.30	161.08
D_{WS} (nm)	18	25
D_{TEM} (nm)	32	61
χ^2 (%)	1.68	1.34

the orthorhombic system with *Pnma* space group. Fig. 2b illustrates the crystal structure of the samples under investigation. The obtained unit cell values of each compound are presented in Table 1.

The average crystallite size was determined according to the Williamson–Hall approach using the following relation:[53–55]

$$\beta \cos \theta = \frac{k\lambda}{D_{WH}} + 4\varepsilon \sin \theta \quad (1)$$

where $k = 0.9$ is a constant, β is the FWHM of a diffraction peak expressed in radians, $\lambda = 1.5406$ Å is the wavelength of Cu K_α radiation, θ is the Bragg's diffraction angle and ε is the microstrain.

Fig. 2c represents the ($\beta \cos \theta$) (y-axis) *vs.* (4 sin θ) (x-axis) data related to the most intense peaks of NSMO-AC and NSMO-SG samples. The crystallite size D_{WH} was deduced from the y-intercept of the linearly fitted data, and the microstrain ε is deduced from the slope. The D_{WH} and ε values were, respectively, equal to 18 nm and 0.0008 for NSMO-AC and 25 nm and 0.0003 for NSMO-SG.

The surface TEM micrographs of the aforementioned compounds are exemplified in the inset of Fig. 3a. It is worth noticing that the shape of the particles differed based on the synthesis route. The size distribution of the grains analyzed quantitatively by fitting the histogram according to a Lorentzian function is depicted in Fig. 3a. The mean diameters of NSMO-AC and NSMO-SG compounds were around 32 and 61 nm, respectively. The particle size determined from the TEM image was higher than that estimated by the XRD experiment, which can be elucidated by the fact that each particle analyzed by TEM was composed of numerous different crystallized grains.

Fig. 3b exhibits the EDAX spectra of NSMO-AC and NSMO-SG compounds, respectively. The analysis was performed on several zones. All the ingredients incorporated within the synthesis (Nd, Sr, Mn, and O) were present. One can see that there are no impurities. The composition of the compound was identical to the desired one.

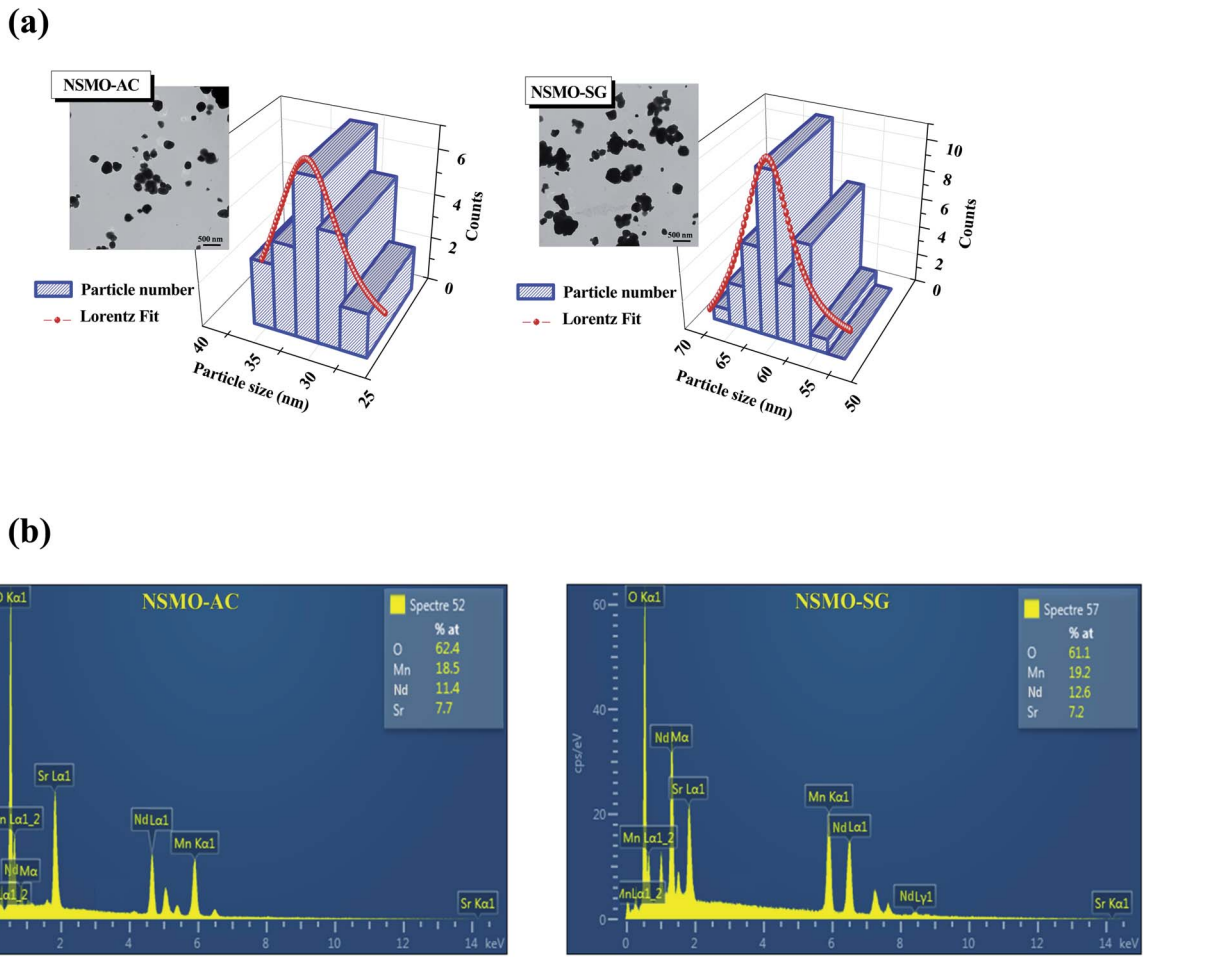

Fig. 3 (a) Size distribution histogram of NSMO-AC and NSMO-SG compounds. The inset presents the TEM image, (b) EDAX analysis spectrum.

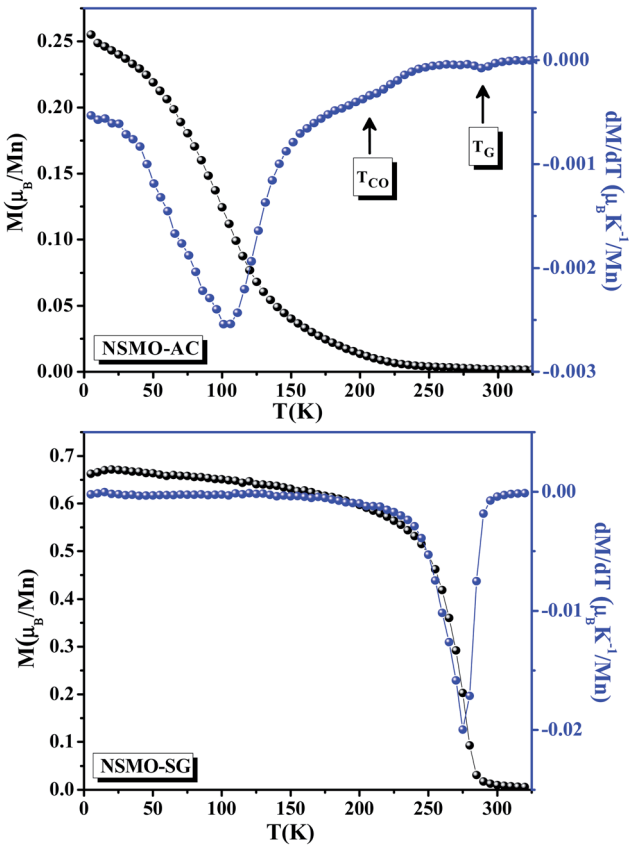

Fig. 4 Magnetization (M) *vs.* temperature and the plot of dM/dT at $\mu_0 H$ = 0.05 T of NSMO-AC and NSMO-SG compounds.

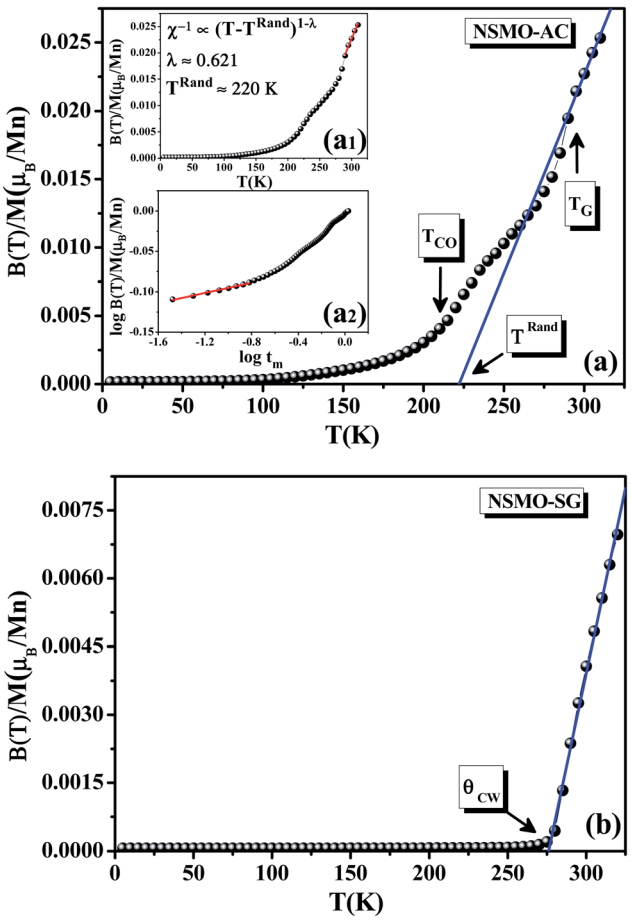

Fig. 5 (a) The inverse magnetic susceptibility *vs.* temperature at $\mu_0 H$ = 0.05 T of NSMO-AC compound (the solid blue line is the linear fit to the susceptibility curve following to Curie–Weiss law in the PM region). The inset displays (a_1) Griffiths power law and (a_2) the double logarithmic plot (the solid red lines are the best linear fits). (b) The inverse magnetic susceptibility *vs.* temperature at $\mu_0 H$ = 0.05 T of NSMO-SG compound (the solid blue line is the linear fit to the susceptibility curve following to Curie–Weiss law in the PM region).

3.2. Magnetic study

Fig. 4 displays the temperature dependence of the magnetization data $M(T)$ carried out at $\mu_0 H$ = 0.05 T for NSMO-AC and NSMO-SG specimens. With an increase in the temperature, both the samples underwent a clear ferromagnetic (FM)–paramagnetic (PM) phase transition at Curie temperature (T_C). The obtained T_C values, equivalent to the minimum of (dM/dT) plot, were 100 and 270 K for NSMO-AC and NSMO-SG samples, respectively. It could be observed that the $M(T)$ curve of the NSMO-AC compound exhibited a drop in the magnetic moment, revealing that the FM order was weaker than that of the NSMO-SG compound.

Fig. 5 presents the temperature dependence of the inverse magnetic susceptibility $\chi^{-1}(T)$ data. The solid blue line was the best fit of Curie Weiss law in the PM region defined as follow:[56,57]

$$\chi^{-1}(T) = \frac{T - \theta_{CW}}{C} \quad (2)$$

where θ_{CW} is the Curie Weiss temperature and C is Curie constant.

For the NSMO-AC sample (Fig. 5a), the $\chi^{-1}(T)$ curve showed a downturn deviation from the Curie Weiss law indicating the existence of a Griffiths phase (GP),[58–60] which corresponded to the appearance of the FM clusters within the PM region in the temperature range $T^{Rand} \leq T \leq T_{GP}$, thereby defining the Griffiths regime. T_{GP} was the temperature at which the $\chi^{-1}(T)$ curve deviated from the Curie Weiss law called the Griffiths temperature.[61] This was also illustrated by the dM/dT plot (Fig. 4). T^{Rand} was the critical temperature of a random FM state called the random transition temperature.[62] T^{Rand} was equivalent to the Curie Weiss temperature (θ_{CW}).

The GP was characterized by an exponent λ, defined by the following equation:

$$\chi^{-1}(T) \propto (T - T^{Rand})^{1-\lambda}; (0 \leq \lambda < 1) \quad (3)$$

Table 2 Curie temperature (T_C), Curie Weiss temperature (θ_{CW}), random transition temperature (T^{Rand}), Griffiths temperature (T_{GP}), charge ordering transition temperature (T_{CO}). Exponent λ indicates the strength of GP for NSMO-AC and NSMO-SG compounds

Compound	T_C (K)	$\frac{T^{Rand}}{\theta_{CW}}$ (K)	T_{GP} (K)	λ	T_{CO} (K)
NSMO-AC	100	220	290	0.621	210
NSMO-SG	275	276	—	—	—

where λ indicates the strength of the GP.[63] The best fit results of the $\chi^{-1}(T)$ data are reported in Fig. 5a$_1$, estimating the values of both λ and T^{Rand}. The obtained parameters are provided in Table 2.

The double logarithmic plot of (χ^{-1}) *vs.* t_m, $t_m = T/T^{Rand} - 1$, reproduced in Fig. 5a$_2$, shows a linear behavior at low t_m values. This result confirms the proposed GP.[64]

The observed slope change, as marked in Fig. 5a, is ascribed to the presence of a charge ordering state (CO).[65,66] As reported in a previous study,[67] the CO transition refers basically to the appearance of an antiferromagnetic (AFM) ordering phase which makes the inverse susceptibility curves plotted upward. T_{CO} is the CO transition temperature (Table 2). It could also be determined from the conspicuous kink in the dM/dT plot (Fig. 4).

However, for the NSMO-SG sample (Fig. 5b), there was no obvious observable downturn or upward deviation. The $\chi^{-1}(T)$ followed the Curie Weiss law. The obtained θ_{CW} value was positive (Table 2), proving the FM behavior of the studied sample.[68,69]

For the NSMO-SG compound, the disappearance of the GP and the CO state was attributed to the enhancement of FM interactions. Each particle was supposed to be composed of two parts.[70] The first one was the core where the double exchange interactions dominated and promoted an FM character. As for the other part, it was a disordered shell where the magnetic interactions were modified by the vacancies, defects as well as broken bonds and disfavored the FM behavior.[71] Therefore, the appearance of the GP and the CO state until the reduction of the crystallite size arose from the loss of the FM order, since the surface contribution was larger.

Isothermal magnetizations *versus* the applied magnetic field $M(\mu_0H,T)$ for NSMO-AC and NSMO-SG samples performed at several temperatures are plotted in Fig. 6. At low temperature values, the $M(\mu_0H,T)$ data of NSMO-AC increased rapidly in the low external magnetic field region and were not as yet saturated for an applied magnetic field as great as 5 T. Contrary to the NSMO-SG compound, the $M(\mu_0H,T)$ data increased sharply in the low magnetic field region and subsequently saturated as the field value increased, which corroborated to the high FM character of the NSMO-SG sample compared to that of the NSMO-AC sample. At high temperature values, the $M(\mu_0H,T)$ data changed linearly with the applied magnetic field. Both compounds showed a PM behavior.

3.3. Magnetocaloric study

According to the Maxwell relations,[72] the magnetic entropy change (ΔS_M), a significant thermodynamic parameter to enquire about the applicability of the studied specimens as magnetic refrigerants, could be calculated indirectly from the isothermal magnetization data using a numerical approximation:

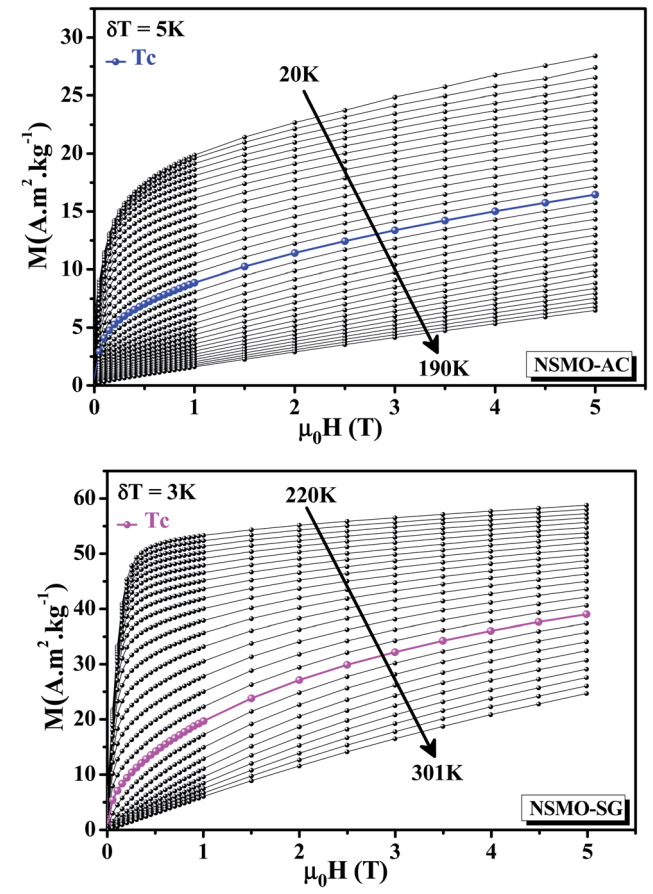

Fig. 6 Isothermal magnetization curves recorded at various temperature values around T_C for NSMO-AC and NSMO-SG compounds.

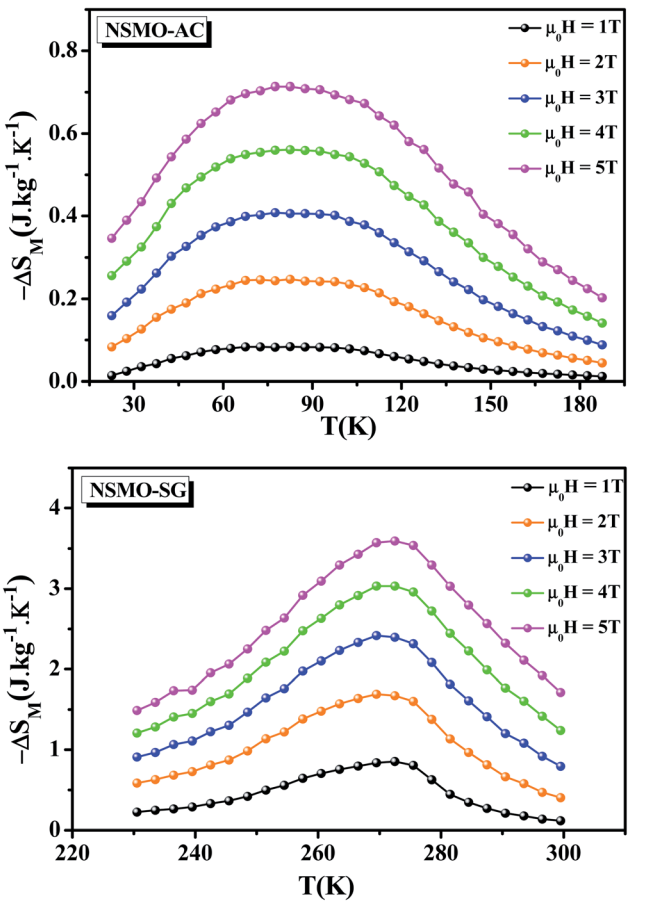

Fig. 7 Magnetic entropy change (ΔS_M) *vs.* temperature at several applied magnetic fields for NSMO-AC and NSMO-SG compounds.

Table 3 Values of the maximum magnetic entropy change (ΔS_M^{max}) and the relative cooling power (RCP) of NSMO-AC and NSMO-SG compounds compared with the other magnetic materials

Compound	$\mu_0 H$ (T)	T_C (K)	$-\Delta S_M^{max}$ (J kg^{-1} K^{-1})	RCP (J kg^{-1})	Ref.
$Nd_{0.6}Sr_{0.4}MnO_3$ (auto-combustion method)	1	100	0.083	7.940	This work
	2		0.247	27.481	
	3		0.408	49.929	
	4		0.56	70.632	
	5		0.713	95.271	
$Nd_{0.6}Sr_{0.4}MnO_3$ (sol–gel method)	1	275	0.853	28.322	This work
	2		1.689	72.105	
	3		2.417	116.637	
	4		3.033	163.900	
	5		3.594	202.054	
Gd	2	—	5.5	164	76
	5		10.2	410	77
$Nd_{0.6}Sr_{0.4}MnO_3$ (solid-state method)	2	245	1.71	74.88	30
	5		3.68	216.03	
$La_{0.6}Sr_{0.4}MnO_3$	2	365	0.97	98	26
	5		2.14	264	
$Nd_{0.50\text{-}0.17}Sr_{0.33}MnO_3$	1	220	0.19	—	29
$Nd_{0.7}Sr0.3MnO3$	2	240	5.3	80	79
$Nd_{0.67}Ba_{0.33}MnO_3$	5	145	3.91	265	78
$Nd_{0.67}Ba_{0.33}Mn_{0.98}Fe_{0.1}O_3$	5	134	2.97	242	78

$$\Delta S_M(T, \mu_0 H_{max}) = \int_0^{\mu_0 H_{max}} \left[\frac{\partial M}{\partial T}\right]_{\mu_0 H} d\mu_0 H \quad (4)$$

The temperature dependence of the magnetic entropy change ($-\Delta S_M(T)$) of NSMO-AC and NSMO-SG compounds, established at various external magnetic fields, is shown in Fig. 7. It was worth noting that the magnitude of ΔS_M increased gradually when the external magnetic field was increased and achieved its maximum around T_C, which was indicative of a much considerable magnetic entropy change to be predicted at higher magnetic field values. For $\mu_0 H = 2$ T, the NSMO-AC sample presented a maximum ΔS_M^{max} value of 0.247 J kg^{-1} K^{-1}, and the NSMO-SG sample reached a maximum ΔS_M^{max} value of 1.689 J kg^{-1} K^{-1}. For $\mu_0 H = 5$ T, the maximum ΔS_M^{max} value was 0.713 J kg^{-1} K^{-1} for the NSMO-AC compound and 3.594 J kg^{-1} K^{-1} for the NSMO-SG compound. Thus, the NSMO-SG compound achieved an important MCE near room temperature with a considerable ΔS_M^{max} value making the system potentially beneficial for magnetic refrigeration applications.

As can be seen, the ΔS_M peak of the NSMO-AC sample was larger than that of the NSMO-SG sample. Such an enlargement of the ΔS_M peak was assigned to the increase in the surface/volume ratio. When the crystallite size reduced, the surface proportion increased, which resulted in a weakness of the FM coupling compared to that of the core. This fact led to a scattering of the Curie temperature values, and thus a broad magnetic transition.[73,74]

The magnetocaloric effectiveness could be assessed through the relative cooling power (RCP),[75] which was defined as the quantity of heat transferred between the hot and the cold sinks in an ideal refrigeration cycle. The latter takes into account the magnitude of (ΔS_M) and its FWHM (δT_{FWHM}). It was calculated as follow:

$$RCP = (-\Delta S_M^{max}) \times \delta T_{FWHM} \quad (5)$$

The obtained RCP was 95.271 J kg^{-1} for NSMO-AC and 202.054 J kg^{-1} for NSMO-SG at $\mu_0 H = 5$ T, which accounted for about 23% and 50% of that estimated in pure gadolinium (Gd), respectively.

To further estimate the efficacy of our compounds in the magnetic cooling systems, the calculated ΔS_M^{max} and the RCP values found in the present study are compared with that of other magnetic materials[26,29,30,76–79] and tabulated in Table 3.

3.4. Critical behavior study

Fig. 8a illustrates the so-called Arrott plots of M^2 *vs.* $\mu_0 H/M$ extracted from the magnetization isotherms following the mean-field model ($\beta = 0.5$ and $\gamma = 1$). In accordance with the assumption of the Banerjee criterion,[80,81] the order of the magnetic transition was defined *via* the sign of the slope of M^2 *vs.* $\mu_0 H/M$ curves. A positive slope was noted for all of the investigated temperatures, which asserted that the FM/PM phase transition was of the second order.

Based on the universal scaling relations, a second-order magnetic transition near the Curie temperature T_C was specified by means of interconnected critical exponents, namely β is the exponent related to the spontaneous magnetization M_S under T_C, γ is the exponent associated with the magnetic susceptibility ${\chi_0}^{-1}$ beyond T_C and δ is the exponent linked to the critical isothermal magnetization at T_C. The critical exponent values were mathematically approximated from the magnetization data *via* the asymptotic formulas as follow:[82]

$$M_S(T < T_C, \mu_0 H \to 0) = M_0 |\varepsilon|^{\beta} \quad (6)$$

$${\chi_0}^{-1}(T > T_C, \mu_0 H \to 0) = \frac{h_0}{M_0} |\varepsilon|^{\gamma} \quad (7)$$

$$M(T = T_C, \mu_0 H) = D(\mu_0 H)^{1/\delta} \quad (8)$$

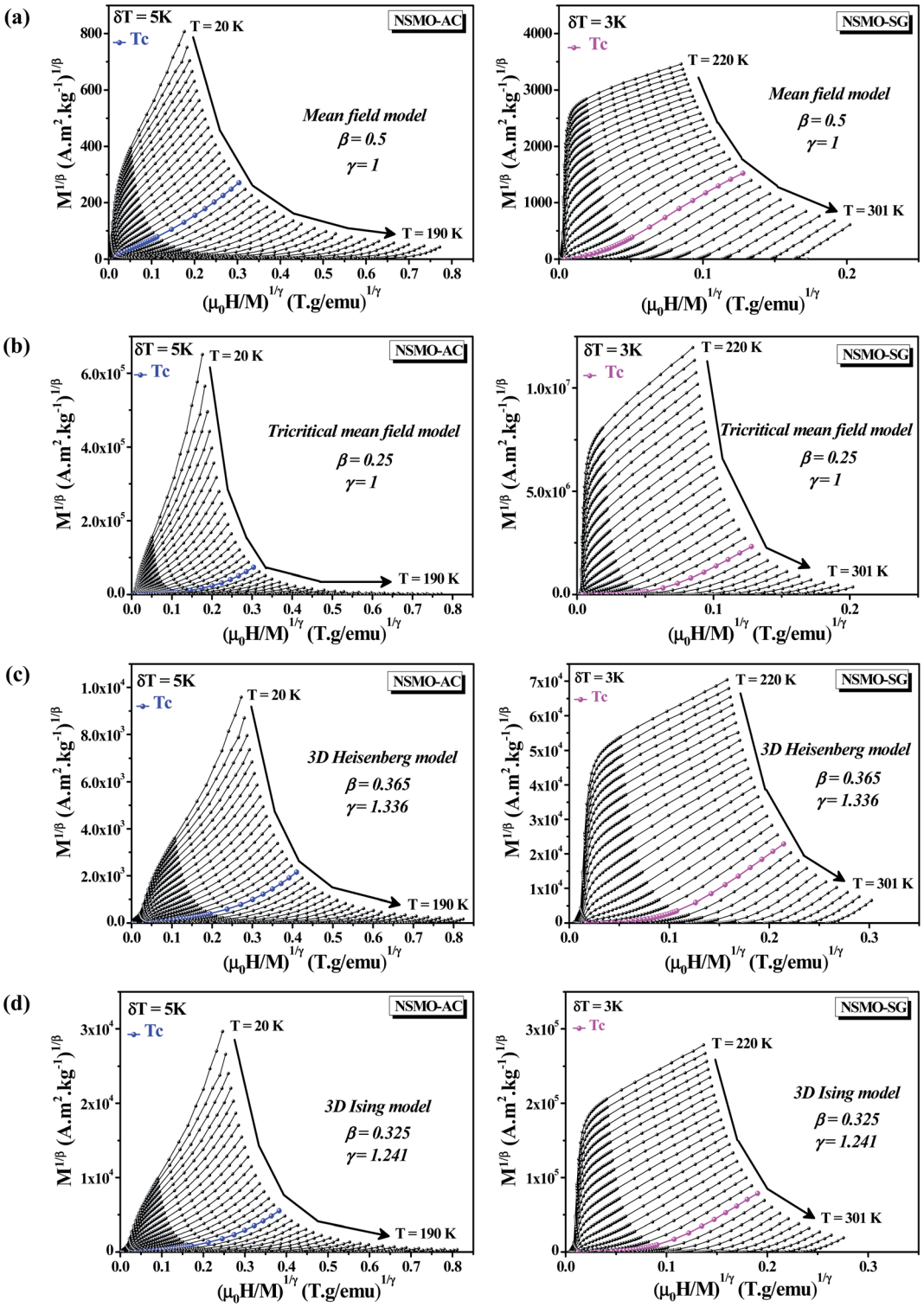

Fig. 8 Modified Arrott plots (MAP): $M^{1/\beta}$ *vs.* $(\mu_0 H/M)^{1/\gamma}$ with (a) mean-field model, (b) tri-critical mean-field model, (c) 3D-Heisenberg model and (d) 3D-Ising model for NSMO-AC and NSMO-SG samples.

where M_0, $\frac{h_0}{M_0}$ as well as D are critical amplitudes and $\varepsilon = \frac{T - T_C}{T_C}$ is the reduced temperature.

According to the Arrott–Noakes equation of state,[83] the experimental data were examined through the modified Arrott-plot (MAP) formula:

$$\left(\frac{\mu_0 H}{M}\right)^{1/\gamma} = a \times \left(\frac{T - T_C}{T}\right) + bM^{1/\beta} \quad (9)$$

where a and b are considered to be constants.

The appropriate model brought about a set of reasonably good parallel straight lines.

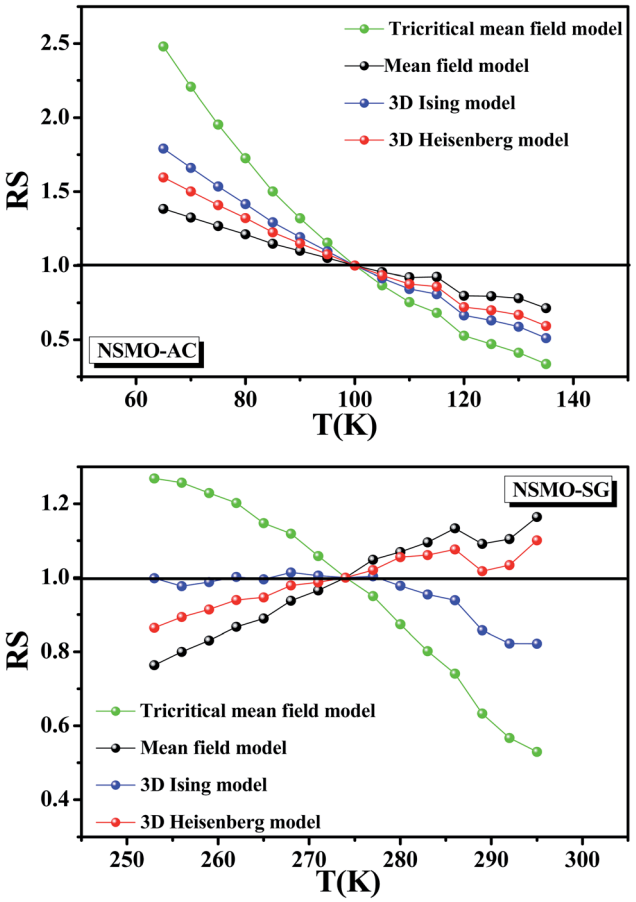

Fig. 9 Relative slope (RS) *vs.* temperature for NSMO-AC and NSMO-SG compounds.

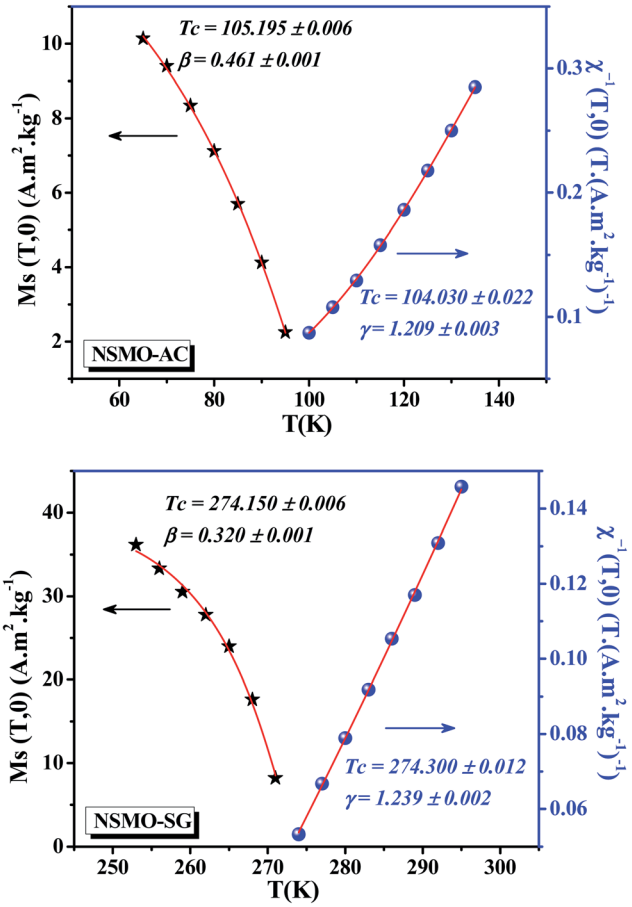

Fig. 10 Spontaneous magnetization $M_S(T)$ and the inverse initial susceptibility $\chi_0^{-1}(T)$ data for NSMO-AC and NSMO-SG compounds. Solid lines correspond to the fitting curves.

Fig. 8 displays the plot of $M^{1/\beta}$ *vs.* $\left(\frac{\mu_0 H}{M}\right)^{1/\gamma}$ at various temperatures using different theoretical models: (a) the mean-field model ($\beta = 0.5$ and $\gamma = 1$), (b) the tri-critical mean-field model ($\beta = 0.25$ and $\gamma = 1$), (c) the 3D-Heisenberg model ($\beta = 0.365$ and $\gamma = 1.336$) and (d) the 3D-Ising model ($\beta = 0.325$ and $\gamma = 1.240$). All models presented nearly parallel lines and quasi straight in the region of high field values. It was complicated to identify the most adequate model to characterize our samples.

Herein, it was essential to calculate the relative slope (RS), which was considered as a new specific indicator to select the suitable model. The RS was expressed at the critical temperature as follow:

$$\mathrm{RS} = \frac{S(T)}{S(T_C)} \tag{10}$$

where $S(T)$ and $S(T_C)$ are the slopes determined from the MAP near and at T_C, respectively.

Fig. 9 presents the RS *vs.* T data of both the systems for the following four models: the mean-field model, the tri-critical mean-field model, the 3D-Heisenberg model and the 3D-Ising model. The most ideal model was the one that presented an RS value equal to 1.[84]

It was clear that the mean-field model was the most satisfactory one to define the critical properties of the NSMO-AC compound, whereas the 3D Ising model was the ideal one to specify the critical behavior of the NSMO-SG compound. The change in the universality class could be associated with the change in the elaboration process, which influenced the crystallite size. Similar results were reported in ref. 85 and 86, where the authors suggested that the reduction in the crystallite size presented an intensive impact on the magnetic interactions and strongly influenced the universality class.

Departing from the MAP, the linear extrapolation of the isotherm in the high magnetic field region provided the spontaneous magnetization M_S values as well as the inverse susceptibility χ_0^{-1} values as intercepts on the coordinate axes $M^{1/\beta}$ and $\left(\frac{\mu_0 H}{M}\right)^{1/\gamma}$, respectively. The $M_S(T)$ and $\chi_0^{-1}(T)$ data are demonstrated in Fig. 10. Using eqn (6) and (7), the best fit results of $M_S(T)$ and $\chi_0^{-1}(T)$ plots, respectively, provide new values of β, γ, and T_C (Table 4).

From Table 4, it is worth highlighting that the obtained critical exponents of NSMO-SG are self-consistent and in accurate estimates when compared with the theoretical ones. However, the estimated critical exponents of NSMO-AC exhibited

Table 4 Critical exponent values of NSMO-AC and NSMO-SG samples

Model/compound	Technique	T_C (K)	β	γ	δ
Mean-field model			0.5	1	3
Tri-critical mean-field model			0.25	1	5
3D-Heisenberg model			0.365	1.336	4.80
3D-Ising model			0.325	1.240	4.82
NSMO-AC	MAP	105.195 ± 0.006	0.461 ± 0.001	1.209 ± 0.003	
	KF	104.167 ± 0.008	0.621 ± 0.002	1.123 ± 0.005	
	CIA (exp.)				2.516 ± 0.038
	CIA (cal.)				2.80
NSMO-SG	MAP	274.150 ± 0.006	0.320 ± 0.001	1.239 ± 0.002	
	KF	273.980 ± 0.001	0.323 ± 0.002	1.235 ± 0.004	
	CIA (exp.)				4.831 ± 0.016
	CIA (cal.)				4.82

a slight deviation from the exponent values predicted for the theoretical interaction models. Generally, for the inhomogeneous FM materials, the values of the critical exponents were incompatible when compared with those of the traditional universality classes. Similar results were reported by Sudakshina *et al.*[87]

A further processing of $M_S(T)$ and $\chi_0^{-1}(T)$ was realized using the Kouvel–Fisher (KF) method[88] so as to determine accurately the values of β, γ, and T_C. The function construction was defined by the following expressions:

$$M_S(T)\left(\frac{dM_S(T)}{dT}\right)^{-1} = \frac{T - T_C}{\beta} \quad (11)$$

$$\chi_0^{-1}(T)\left(\frac{d\chi_0^{-1}(T)}{dT}\right)^{-1} = \frac{T - T_C}{\gamma} \quad (12)$$

Under this method, the plots of $M_S(T)\left(\frac{dM_S(T)}{dT}\right)^{-1}$ and $\chi_0^{-1}(T)\left(\frac{d\chi_0^{-1}(T)}{dT}\right)^{-1}$, shown in Fig. 11, appear as straight lines

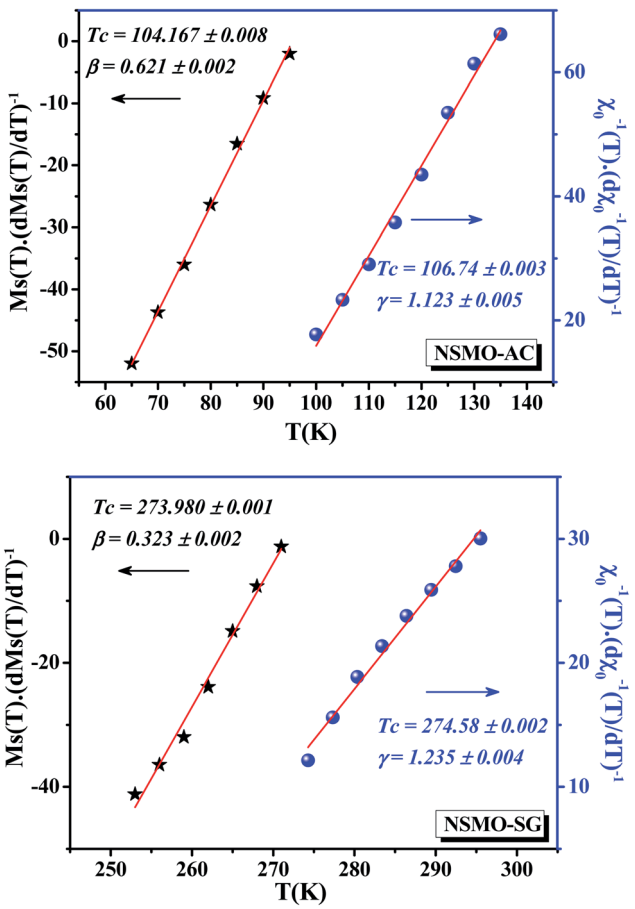

Fig. 11 Kouvel–Fisher (KF) curves for the spontaneous magnetization $M_S(T)$ and the inverse initial susceptibility $\chi_0^{-1}(T)$ of NSMO-AC and NSMO-SG compounds. Solid lines correspond to the linear fits.

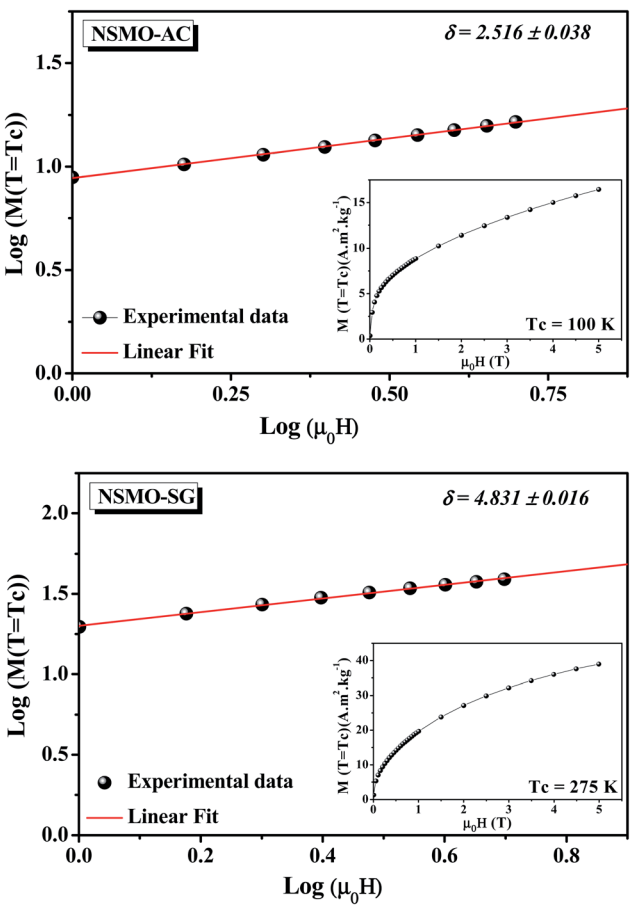

Fig. 12 Critical isotherm (M *vs.* $\mu_0 H$), plotted on a log–log scale, for NSMO-AC and NSMO-SG compounds.

with $1/\beta$ and $1/\gamma$ slopes, respectively. The intercepts on the T axis of their extrapolation to the ordinate equal to zero corresponding to the T_C values. It was noted that the critical exponent as well as the Curie temperature values determined from the KF method (Table 4) go in tandem with those deduced from the MAP. Consequently, we could conclude that the aforementioned methods were feasible and effective to investigate the critical properties.

Fig. 12 presents the critical isotherm (M *vs.* $\mu_0 H$) curves at T_C = 100 and 275 K for NSMO-AC and NSMO-SG, respectively, plotted on a log–log scale. By fitting the $M(\mu_0 H)$ with eqn (8), the third exponent δ value is achieved. The obtained values, recapitulated in Table 4, are similar to those calculated theoretically through the Widom scaling law:[89]

$$\delta = 1 + \frac{\gamma}{\beta} \tag{13}$$

These findings validated the exactness of the calculated values of β and γ.

For more certainity, the reliability of the acquired critical exponents could be determined through the universal scaling theory around the critical region, which could be described by the equation below:

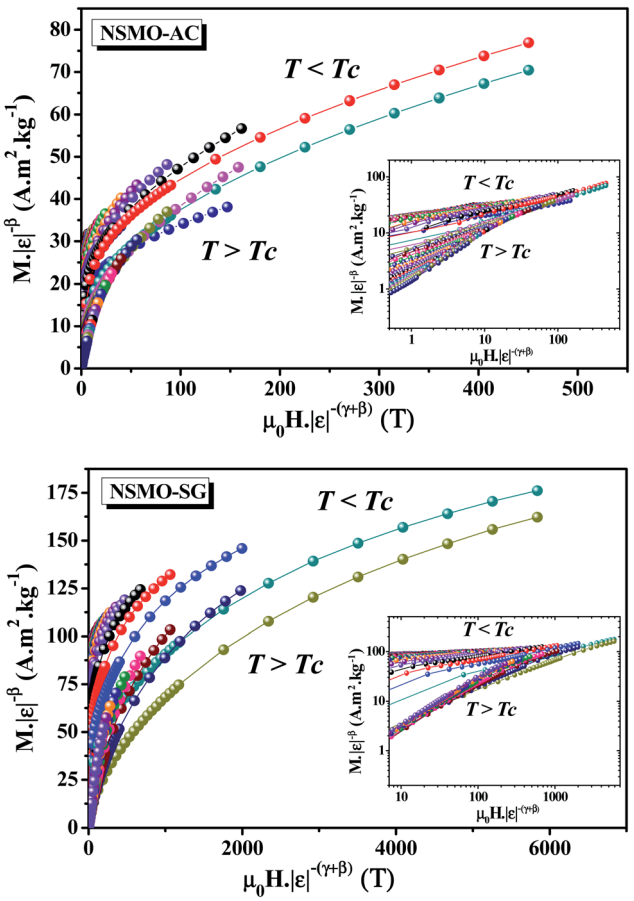

Fig. 13 Scaling plots $M|\varepsilon|^{-\beta}$ *vs.* $\mu_0 H|\varepsilon|^{-\beta-\gamma}$ around T_C for NSMO-AC and NSMO-SG samples. The inset depicts the same plots on the log–log scale.

$$M(\mu_0 H, \varepsilon) = |\varepsilon|^{\beta} f_{\pm}\left(\frac{\mu_0 H}{|\varepsilon|^{\beta+\gamma}}\right) \tag{14}$$

where $f_-(T < T_C)$ and $f_+(T > T_C)$ are regular functions.

Fig. 13 displays the plot of $M|\varepsilon|^{-\beta}$ *vs.* $\mu_0 H|\varepsilon|^{-\beta-\gamma}$ by using β, γ, and T_C values determined by the KF method. It can be obviously seen that all of the experimental data fell into two independent branches around T_C. This observation ensured that eqn (14) is obeyed, which denotes the accuracy of the obtained critical exponents and that of the Curie temperature.

4. Conclusion

In summary, a detailed study of the structural, magnetic, magnetocaloric, and critical behavior of the $Nd_{0.6}Sr_{0.4}MnO_3$ compound was systematically performed. The sample was synthesized by using two different methods: the auto-combustion method (NSMO-AC) and the sol–gel process (NSMO-SG). Rietveld refinements of the XRD data indicated that the studied samples adopted an orthorhombic structure with *Pnma* space group. Both compounds exhibited a second-order phase transition from FM to PM state at T_C. The appearance of a Griffiths phase (GP), as well as a charge ordering state (CO) in the compound prepared by the auto-combustion reaction, was explained in terms of the core–shell model. The specimen elaborated by the sol–gel method presented a greater magnetic entropy change value than that presented by the sample synthesized by the auto-combustion process, which made it a suitable material for the magnetic refrigeration device. The critical behavior related to the FM/PM phase transition implied that the calculated exponents were in good agreement with the prediction of the mean-field model and the 3D-Ising model for NSMO-AC and NSMO-SG samples, respectively, which proved that the synthesis route played a significant role in changing the universality class.

Conflicts of interest

There are no conflicts to declare.

Acknowledgements

The authors acknowledge the Taif University Research Supporting Project (TURSP-2020/66), Taif University, Taif, Saudi Arabia.

References

1 A. Kitanovski, *Adv. Energy Mater.*, 2020, **10**, 1903741.
2 A. Kitanovski, J. Tušek, U. Tomc, U. Plaznik, M. Ozbolt and A. Poredoš, *Magnetocaloric Energy Conversion: From Theory to Applications*, Springer, 2014.
3 O. Gutfleisch, M. A. Willard, E. Bruck, C. H. Chen, S. G. Sankar and J. P. Liu, *Adv. Mater.*, 2011, **23**, 821.
4 E. L. T. França, A. O. dos Santos, A. A. Coelho and L. M. da Silva, *J. Magn. Magn. Mater.*, 2016, **401**, 1088.

5 C. Romero-Muniz, V. Franco and A. Conde, *Phys. Chem. Chem. Phys.*, 2017, **19**, 3582.
6 M. Balli, S. Jandl, P. Fournier, S. Mansouri, A. Mukhin, Y. V. Ivanov and A. M. Balbashov, *J. Magn. Magn. Mater.*, 2015, **374**, 252.
7 Y. Yi, L. Li, K. Su, Y. Qi and D. Huo, *Intermetallics*, 2017, **80**, 22.
8 Y. Yang, Y. Zhang, X. Xu, S. Geng, L. Hou, X. Li, Z. Ren and G. Wilde, *J. Alloys Compd.*, 2017, **692**, 665.
9 Y. Zhang, L. Hou, Z. Ren, X. Li and G. Wilde, *J. Alloys Compd.*, 2016, **656**, 635.
10 M. H. Phan and S. C. Yu, *J. Magn. Magn. Mater.*, 2007, **308**, 325.
11 M. Smari, I. Walha, E. Dhahri and E. K. Hlil, *J. Alloys Compd.*, 2013, **579**, 564.
12 S. Xi, W. Lu and Y. Sun, *J. Appl. Phys.*, 2012, **111**, 063922.
13 M. Bejar, R. Dhahri, F. ElHalouani and E. Dhahri, *J. Alloys Compd.*, 2006, **414**, 31.
14 A. Dhahri, M. Jemmali, E. Dhahri and M. A. Valente, *J. Alloys Compd.*, 2015, **638**, 221.
15 M. Khlifi, M. Bejar, E. Dhahri, P. Lachkar and E. K. Hlil, *J. Appl. Phys.*, 2012, **111**, 103909.
16 R. Skini, A. Omri, M. Khlifi, E. Dhahri and E. K. Hlil, *J. Magn. Magn. Mater.*, 2014, **364**, 5.
17 Y. Tokura, *Rep. Prog. Phys.*, 2006, **69**, 797.
18 N. Dhahri, A. Dhahri, K. Cherif, J. Dhahri, K. Taibi and E. Dhahri, *J. Alloys Compd.*, 2010, **496**, 69.
19 A. Tozri, E. Dhahri and E. K. Hlil, *J. Mater. Lett.*, 2010, **64**, 2138.
20 M. Khlifi, A. Tozri, M. Bejar, E. Dhahri and E. K. Hlil, *J. Magn. Magn. Mater.*, 2012, **324**, 2142.
21 M. Jeddi, H. Gharsallah, M. Bejar, M. Bekri, E. Dhahri and E. K. Hlil, *RSC Adv.*, 2018, **8**, 9430.
22 P. Gupta and P. Poddar, *RSC Adv.*, 2015, **5**, 10094.
23 I. A. Abdel-Latif, *J. Alloys Compd.*, 2008, **245**, 452.
24 I. A. Abdel-Latif, A. S. Khramov, V. A. Trounov, O. P. Smirnov, S. S. Bashkirov, V. V. Parfenov and S. Z. Ibragimov, *Egypt. J. Solids*, 2006, **29**, 341.
25 H. Gharsallah, M. Bejar, E. Dhahri and E. K. Hlil, *Mater. Chem. Phys.*, 2016, **182**, 429.
26 M. Jeddi, H. Gharsallah, M. Bekri, E. Dhahri and E. K. Hlil, *RSC Adv.*, 2018, **8**, 28649.
27 M. Jeddi, H. Gharsallah, M. Bekri, E. Dhahri and E. K. Hlil, *Appl. Phys. A: Mater. Sci. Process.*, 2020, **126**, 6.
28 B. Arun, M. V. Suneesh, B. Sudakshina, V. R. Akshay, K. D. Chandrasekhar and M. Vasundhara, *J. Phys. Chem. Solids*, 2018, **123**, 327.
29 B. Arun, V. R. Akshay, K. D. Chandrasekhar, G. R. Mutta and M. Vasundhara, *J. Magn. Magn. Mater.*, 2019, **472**, 74–85.
30 F. Issaoui, E. Dhahri and E. K. Hlil, *J. Low Temp. Phys.*, 2020, **200**, 15.
31 N. Assoudi, I. Walha, K. Nouri, E. Dhahri and L. Bessais, *J. Alloys Compd.*, 2018, **753**, 282.
32 K. Riahi, I. Messaoui, W. Cheikhrouhou-Koubaa, S. Mercone, B. Leridon, M. Koubaa and A. Cheikhrouhou, *J. Alloys Compd.*, 2016, **688**, 1028.
33 K. A. Bouziane, *J. Appl. Phys.*, 2005, **97**, 504.
34 A. A. Yousif, *AIP Conf. Proc.*, 2011, **1370**, 103.
35 I. A. Abdel-Latif and S. A. Saleh, *J. Alloys Compd.*, 2012, **530**, 116.
36 Y. Cui, *Ceram. Int.*, 2012, **38**, 4761.
37 Z. F. Zi, *J. Magn. Magn. Mater.*, 2009, **321**, 2378.
38 I. A. Abdel-Latif, *AIP Conf. Proc.*, 2011, **1370**, 108.
39 M. A. Basith, B. Ahmmad, S. Hossain and K. Molhave, *Mater. Res. Express*, 2017, **4**, 075012.
40 P. Žvátora, *J. Solid State Chem.*, 2013, **204**, 373.
41 K. N. Anuradha, *IOP Conf. Ser.: Mater. Sci. Eng.*, 2015, **73**, 012007.
42 Y. Romaguera-Barcelay, *J. Electroceram.*, 2011, **26**, 44.
43 A. Mleiki, *J. Alloys Compd.*, 2017, **727**, 1203.
44 M. Verelst, N. Rangavittal, C. N. R. Rao and A. Rousset, *J. Solid State Chem.*, 1993, **104**, 74.
45 M. Gupta, P. Yadav, W. Khan, A. Azam, A. H. Naqvi and R. K. Kotnala, *Adv. Mater. Lett.*, 2012, **3**, 220.
46 A. C. F. M. Costa, M. R. Morelli and R. H. G. A. Kiminami, *J. Mater. Sci.*, 2007, **42**, 779.
47 M. George, A. Mary John and S. S. Nair, *J. Magn. Magn. Mater.*, 2006, **302**, 190.
48 A. S. Mukasyan, P. Epstein and P. Dinka, *Proc. Combust. Inst.*, 2007, **31**, 1789.
49 K. Abdouli, W. Cherif, E. Kadri, K. Dhahri, P. R. Prezas, M. P. F. Graça and L. Ktari, *J. Alloys Compd.*, 2018, **739**, 1048.
50 S. B. Moumen, Y. Gagou, M. Chettab, D. Mezzane, M. Amjoud and S. Fourcade, *J. Mater. Sci.: Mater. Electron.*, 2019, **30**, 20459.
51 C. Zhu, A. Nobuta, I. Nakatsugawa and T. Akiyama, *Int. J. Hydrogen Energy*, 2013, **38**, 13238.
52 J. Rodrigues-Carvajal, *FULLPROF: A Rietveld Refinement and Pattern Matching Analysis Program*, CEA-CNRS, France, 2000.
53 N. Zaidi, S. Mnefgui, J. Dhahri and E. K. Hlil, *J. Magn. Magn. Mater.*, 2017, **432**, 511–518.
54 P. Goel and K. L. Yadav, *J. Mater. Sci.*, 2007, **42**, 3928.
55 Z. Mohamed, M. Abassi, E. Tka, J. Dhahri and E. K. Hlil, *J. Alloys Compd.*, 2015, **646**, 23.
56 H. Gharsallah, A. Souissi, M. Bejar, E. Dhahri and E. K. Hlil, *Mater. Chem. Phys.*, 2016, **182**, 429–438.
57 A. Tozri, J. Khelifi, E. Dhahri and E. K. Hlil, *Mater. Chem. Phys.*, 2015, **149**, 728.
58 A. Karmakar, S. Majumdar, S. Kundu and T. K. Nath, *J. Phys.: Condens. Matter*, 2012, **24**, 126003.
59 R. B. Griffiths, *Phys. Rev. Lett.*, 1969, **23**, 17.
60 H. Baaziz, A. Tozri, E. Dhahri and E. K. Hlil, *J. Magn. Magn. Mater.*, 2016, **403**, 181.
61 B. Sanjib, B. Nasrin and I. Das, *J. Alloys Compd.*, 2018, **745**, 753.
62 J. Wanjun, Z. XueZhi, W. Gwyn, Y. Mukovskii and R. Privezentsev, *J. Appl. Phys.*, 2010, **107**, 09D701.
63 W. J. Jiang, X. Zhou and G. Williams, *Europhys. Lett.*, 2008, **84**, 47009.
64 X. Zheng, T. Gao, W. Jing, X. Wang, Y. Liu, B. Chen and V. V. Marchenkov, *J. Magn. Magn. Mater.*, 2019, **491**, 165611.
65 T. F. Hiroyuki, H. Fujishiro and M. Ikebe, *J. Phys. Soc. Jpn.*, 1998, **67**, 2582.
66 J. G. R. Klingeler, R. Gross, L. Pinsard-Gaudart, A. Revcolevschi, S. Uhlenbruck and B. Büchner, *Phys. Rev. B: Condens. Matter Mater. Phys.*, 2002, **65**, 174404.

67 S. M. Zhou, Y. Q. Guo, J. Y. Zhao, S. Y. Zhao and L. Shi, *Appl. Phys. Lett.*, 2010, **96**, 262507.
68 A. Sagdeo, K. Gautam, P. R. Sagdeo, M. N. Singh, S. M. Gupta, A. K. Nigam, R. Rawat, A. K. Sinha, H. Ghosh, T. Ganguli and A. Chakrabarti, *Appl. Phys. Lett.*, 2014, **105**, 042906.
69 F. Issaoui, M. T. Tlili, M. Bejar, E. Dhahri and E. K. Hlil, *J. Supercond. Novel Magn.*, 2012, **25**, 1169.
70 H. Baaziz, A. Tozri, E. Dhahri and E. K. Hlil, *J. Magn. Magn. Mater.*, 2016, **403**, 181.
71 M. Secu, M. Cernea, C. E. Secu and B. S. Vasile, *Mater. Chem. Phys.*, 2015, **151**, 81.
72 A. Omri, M. Bejar, M. Sajieddine, E. Dhahri, E. K. Hlil and M. Es-Souni, *Phys. B*, 2012, **407**, 2566.
73 M. Pekala, V. Drozd, J. F. Fagnard and P. Vanderbemden, *J. Alloys Compd.*, 2010, **507**, 350.
74 H. Baaziz, A. Tozri, E. Dhahri and E. K. Hlil, *Ceram. Int.*, 2015, **41**, 2955.
75 V. M. Andrade, R. C. Vivas, S. S. Pedro, J. C. G. Tedesco, A. L. Rossi, A. A. Coelho and M. S. Reis, *Acta Mater.*, 2016, **102**, 49.
76 S. Y. Dankov, A. M. Tishin, V. K. Pecharsky and K. A. Gschneidner Jr, *Phys. Rev. B: Condens. Matter Mater. Phys.*, 1998, **57**, 3478.
77 K. A. Gschneidner Jr, V. K. Pecharsky and A. O. Tsokol, *Rep. Prog. Phys.*, 2005, **68**, 1479.
78 A. M. Ahmed, H. F. Mohamed, A. K. Diab, S. A. Mohamed, S. García-Granda and D. Martínez-Blanco, *Solid State Sci.*, 2016, **57**, 1.
79 S. Hcini, M. Boudard, S. Zemni and M. Oumezzine, *Ceram. Int.*, 2014, **40**, 16041.
80 S. K. Banerjee, *Phys. Lett.*, 1964, **12**, 16.
81 A. Tozri, J. Khelifi, E. Dhahri and E. K. Hlil, *Mater. Chem. Phys.*, 2015, **149**, 728.
82 K. Huang, *Statistical Mechanics*, Wiley, New York, 1987.
83 A. Arrott and J. E. Noakes, *Phys. Rev. Lett.*, 1967, **19**, 786.
84 A. Schwartz, M. Scheffler and S. M. Anlage, *Phys. Rev. B: Condens. Matter Mater. Phys.*, 2000, **61**, R870.
85 S. Mahjoub, M. Baazaoui, E. K. Hlil and M. Oumezzine, *Ceram. Int.*, 2015, **41**, 12407.
86 H. Gharsallah, M. Bejar, E. Dhahri and E. K. Hlil, *J. Phys. Chem. Solids*, 2017, **109**, 50.
87 B. Sudakshina, *J. Phys. D: Appl. Phys.*, 2017, **50**, 065004.
88 J. S. Kouvel and M. E. Fisher, *Phys. Rev. B: Solid State*, 1964, **136**, A1626.
89 B. Widom, *J. Chem. Phys.*, 1965, **43**, 3898.